ACS OMEGA

Open Access

http://pubs.acs.org/journal/acsodf

Article

Demonstration of the Effectiveness of the Cascaded Variational Quantum Eigensolver Using the Jastrow Ansatz for Molecular Calculations

John P. T. Stenger,* C. Stephen Hellberg, and Daniel Gunlycke

Cite This: *ACS Omega* 2024, 9, 21353−21364

Read Online

ACCESS | Metrics & More | Article Recommendations

ABSTRACT: We demonstrate how the cascaded variational quantum eigensolver (CVQE) can be applied to study molecular systems for the family of Jastrow ansatzes. Specifically, we applied CVQE to the water molecule. We find that CVQE has a number of advantages. In particular, our results show that CVQE requires 2 to 3 orders of magnitude fewer quantum computing (QC) executions than VQE for the water molecule. Furthermore, our results indicate that CVQE might provide some robustness against two-qubit gate errors given that the number of CNOT gates used in our calculation was ∼300 and the errors in the QC calculations are still comparable to those obtained by VQE.

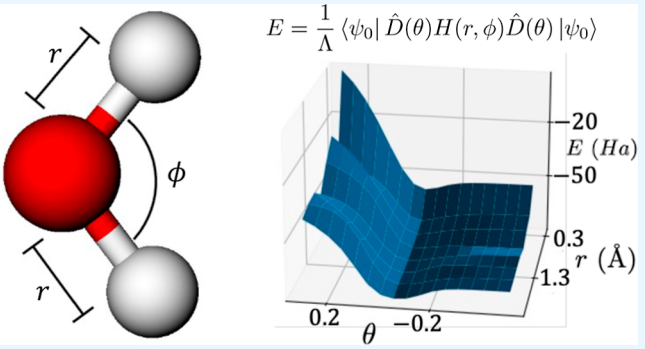

1. INTRODUCTION

The properties of a molecule can generally be determined from its electronic ground state. Solving for the many-electron ground state, however, is an exponentially hard task as the size of the Fock space increases exponentially with the number of spin orbitals. Consequently, classical electronic structure methods must use approximations for all systems but the smallest systems. In contrast, quantum computing (QC) may allow us to avoid approximations as the full Fock space can be represented in a quantum register composed of a number of qubits proportional to the number of spin orbitals.[1,2]

Present day quantum computers are limited by environmental noise, errors in implementing gate operations, and read-out errors. The variational quantum eigensolver (VQE)[3−13] seeks to address some of these limitations. VQE is a method to solve for the ground-state energy of molecules by using quantum circuits composed of relatively few quantum logic gates. The small number of quantum logic gates allows the quantum circuit to run quickly, thus avoiding limitations arising from short relaxation times. A downside of VQE is that it requires many circuit executions. Thus, VQE suffers from a different limitation, namely, that there are a limited number of QC resources available and that the competition for computation time is high.

We can address both the issue of short relaxation times and resource scarcity using the cascaded variational quantum eigensolver (CVQE). Unlike VQE, CVQE does not require circuit executions to be repeated throughout the parameter optimization process.[14,15] Instead, measurement samples obtained from the quantum computer are processed on a classical computer according to a variational ansatz. A natural choice of ansatz for CVQE is the Jastrow ansatz.[6,15−36] The Jastrow ansatz has been used in VQE-type algorithms in the past. However, because the Jastrow operator is nonunitary, special care needs to be taken when employing the ansatz for QC. Previous methods for employing the Jastrow ansatz for QC include adding auxiliary qubits,[37,38] approximating the operator,[37,39] and unitarization of the operator.[32,35,40] CVQE allows us to employ the Jastrow operator without auxiliary qubits, approximations, or unitarization.

Herein, we explore the effectiveness of CVQE for studying molecules using the Jastrow ansatz. In particular, we focus on the water molecule. The insights we gain from studying the water molecule can be extended to other molecules. We use both the full Jastrow operator[16] and a specific form of the Jastrow operator that has only a single variational parameter. We compare the single-parameter ansatz to the full Jastrow ansatz and discuss the types of Hamiltonian terms that are well-described using each. Furthermore, we compare CVQE using the Jastrow ansatz to VQE using a hardware efficient (HE) ansatz.[6] We show that CVQE requires many fewer circuit executions than VQE. We also find that we are able to

Received: February 20, 2024
Revised: April 8, 2024
Accepted: April 10, 2024
Published: May 2, 2024

Table 1. CVQE Algorithm Using the Jastrow Ansatz

1:	initialize the quantum register to $\|\Psi_n\rangle$
2:	apply Thouless operator $\hat{U}$ on the quantum computer
3:	collect samples of measurements of $\hat{U}\|\Psi_n\rangle$
4:	using the measurement samples of the quantum computer, compute $E(\theta)$ and $E(\theta + d\theta)$
5:	evaluate $g = \alpha[E(\theta + d\theta) - E(\theta)]$
6:	if $g < \epsilon$, return $E(\theta)$, else, $\theta = \theta - gd\theta$ and go to step 4

implement many more quantum gates using the CVQE method than would be expected from the gate errors, suggesting that the postprocessing in CVQE is compensating for some of the quantum hardware errors.

The remainder of the article has the following outline: Section 2 describes the methods used throughout this work; Section 3 presents the results of our demonstration using the water molecule. Some concluding remarks are provided in Section 4.

2. METHODS

CVQE uses an ansatz of the form

$$|\Psi(\theta)\rangle = \hat{D}(\theta)\hat{U}|\Psi_0\rangle \tag{1}$$

where $\hat{D}(\theta)$ is a diagonal operator, which is applied during the classical processing, θ is a collection of variational parameters, $\hat{U}$ is a unitary operator, which is applied to the quantum computer, and $|\Psi_0\rangle$ is the initial state of the quantum computer. The goal is to compute the energy expectation value

$$E(\theta) = \frac{\langle\Psi(\theta)|\hat{H}|\Psi(\theta)\rangle}{\langle\Psi(\theta)|\Psi(\theta)\rangle} \tag{2}$$

of a Hamiltonian $\hat{H}$. Given the measurement results of the quantum state $\hat{U}|\Psi_0\rangle$, an analytical equation for $E(\theta)$ can be derived that is efficiently computable on a classical computer.[14,15] The efficiency of the calculation is due to $\hat{D}(\theta)$ being diagonal. As long as $\hat{D}(\theta)$ contains only operators that are diagonal in the initial basis of the quantum computer, the energy expectation value $E(\theta)$ can be calculated from sample distributions measured in the same number of bases required to calculate $\langle\Psi_0|\hat{H}|\Psi_0\rangle$. Thus, as long as $\hat{H}$ contains subexponential terms and $\hat{D}(\theta)$ is diagonal, $E(\theta)$ is efficient to calculate. We use the Jastrow ansatz to define $\hat{D}(\theta)$ and $\hat{U}$.[15] The form of the Jastrow ansatz motivates partitioning the Hamiltonian into single-particle, diagonal two-particle, and off-diagonal two-particle terms. We show that each Hamiltonian term is treated differently by the ansatz.

2.1. Jastrow Ansatz. We will now define $\hat{U}$ and $\hat{D}(\theta)$ such that the CVQE ansatz (1) becomes the Jastrow ansatz. Consider a quantum computer composed of Q qubits indexed by the set $Q = \{0, 1, ..., Q - 1\}$. We set the unitary operator to the Thouless operator[41]

$$\hat{U} = \exp[\sum_{qq' \in Q} (\ln f)_{qq'} \hat{c}_q^\dagger \hat{c}_q] \tag{3}$$

where $\hat{c}_q^\dagger$ and $\hat{c}_q$ change the state of qubit q and f transforms the index basis. The operators $\hat{c}_q^\dagger$ and $\hat{c}_q$ are related to the Fermionic creation and destruction operators through a given transformation, i.e., the Jordan–Wigner (JW) transformation.[42] The matrix f has the property

$$\hat{a}_q^\dagger = \sum_{q'} f_{qq'} \hat{c}_{q'}^\dagger \tag{4}$$

where $\hat{a}_q^\dagger$ is the transformation of a creation operator in a new basis. The Thouless operator has the property

$$\begin{aligned} |\Psi_n\rangle &= \prod_{q \in Q} (\hat{c}_q^\dagger)^{n_q} |0\rangle, \\ \hat{U}|\Psi_n\rangle &= \prod_{q \in Q} (\hat{a}_q^\dagger)^{n_q} |0\rangle, \end{aligned} \tag{5}$$

for all families of occupation numbers $n = (n_q)_{q \in Q}$ in the Cartesian power $\mathcal{N} = \{0, 1\}^Q$, where $|0\rangle$ is the vacuum state. Thus, we can use the Thouless operator to change the basis of any given occupation state.

The $\hat{D}(\theta)$ operator must be diagonal on the initial basis of the quantum computer. We choose the Jastrow operator[16,17]

$$\hat{D}(\theta) = \exp(-\sum_{qq' \in Q} \theta_{qq'} \hat{n}_q \hat{n}_{q'}) \tag{6}$$

where $\hat{n}_q = \hat{c}_q^\dagger \hat{c}_q$ is the transformation of the number operator and $\theta_{qq'}$ is a real-valued variational parameter in the collection $\theta = (\theta_{qq'})_{qq' \in Q}$. The accuracy of our method can be systematically improved by including higher-order interaction terms in eq 6. However, for the purposes of this work, we will limit the operator to second-order interactions.

We initialize the system on the Hartree–Fock (HF) basis so that n_q is the occupation of the HF orbital q. We initialize to the state with the lowest N_e spin orbitals occupied, where N_e is the number of electrons. We then use the Thouless operator to rotate into the basis where the noninteracting part of the Hamiltonian is diagonal. The Jastrow operator $\hat{D}(\theta)$ is applied postmeasurement to account for interactions.

2.2. Defining the Hamiltonian for Use with the Jastrow Ansatz. In order to apply the Jastrow ansatz, we need to solve the noninteracting part of the Hamiltonian. Therefore, we need to separate the Full-CI (FCI) Hamiltonian into interacting and noninteracting parts

$$\hat{H} = \hat{H}_1 + \hat{H}_2 \tag{7}$$

where $\hat{H}_1$ contains only single-particle excitations

$$\hat{H}_1 = \sum_{pq \in Q} h_{pq}^1 \hat{c}_p^\dagger \hat{c}_q \tag{8}$$

and $\hat{H}_2$ contains two-particle excitations

$$\hat{H}_2 = \sum_{pqrs} h_{pqrs}^2 \hat{c}_p^\dagger \hat{c}_q^\dagger \hat{c}_r \hat{c}_s \tag{9}$$

where h_{pq}^1 and h_{pqrs}^2 are coefficients given by $\hat{H}$. The noninteracting Hamiltonian $\hat{H}_1$ can be efficiently diagonalized classically. The eigenstates of $\hat{H}_1$ are used to form the matrix f. When f is formed in this way, the operators $\hat{a}_q^\dagger$ create electrons which occupy the eigenstates of $\hat{H}_1$.

https://doi.org/10.1021/acsomega.4c01642
ACS Omega 2024, 9, 21353−21364

For the purpose of our demonstration, it is helpful to also separate the interacting Hamiltonian into diagonal and off-diagonal pieces

$$\hat{H}_2 = \hat{H}_{2D} + \hat{H}_{2F} \tag{10}$$

where $\hat{H}_{2D}$ contains all of the diagonal two-particle operators

$$\hat{H}_{2D} = \sum_{pq \in Q} h_{pq}^{2D} \hat{n}_p \hat{n}_q \tag{11}$$

and $\hat{H}_{2F}$ contains all of the off-diagonal two-particle operators

$$\hat{H}_{2F} = \sum_{pqrs} h_{pqrs}^{2F} \hat{c}_p^\dagger \hat{c}_q^\dagger \hat{c}_r \hat{c}_s \tag{12}$$

where h_{pq}^{2D} and h_{pqrs}^{2F} are coefficients given by $\hat{H}_2$. The coefficient h_{pqrs}^{2F} is defined to have the property that $h_{pqrs}^{2F} = 0$ when $\hat{c}_p^\dagger \hat{c}_q^\dagger \hat{c}_r \hat{c}_s$ can be written as a product of two number operators.

For the water molecule, we find that $\sum_{pq}|h_{pq}^1| > \sum_{pq}|h_{pq}^{2D}| > \sum_{pqrs}|h_{pqrs}^{2F}|$ (see Appendix D). This hierarchy is beneficial for our method as each of these types of terms is handled differently. The Hamiltonian $\hat{H}_1$ is solved by the Thouless operator. We show below that the interactions in the diagonal Hamiltonian $\hat{H}_{2D}$ can be handled using a single-parameter ansatz. The interactions in the off-diagonal Hamiltonian $\hat{H}_{2F}$ require the full Jastrow ansatz. Furthermore, because we use $\hat{D}(\theta)$ to incorporate interactions into the ansatz, and because $\hat{D}(\theta)$ must be diagonal, we expect $\sum_{pq}|h_{pq}{}^{2D}| > \sum_{pqrs}|h_{pqrs}{}^{2F}|$ to be highly important to the success of our algorithm in all cases.

2.3. Overview of the Algorithm. Table 1 shows the steps of the CVQE algorithm. We begin, in step 1, by initializing the quantum register to $|\Psi_n\rangle$, see eq 5, where n is set so that the lowest N_e spin orbitals are filled. In step 2, we apply the Thouless operator to the quantum computer. See reference 15[15] for a detailed description of how to form $\hat{U}$ out of standard quantum gates. In step 3, we collect measurement samples of the quantum state. As shown in references 14[14] and 15,[15] the number of measurements we need is exactly the same as the number of measurements required to calculate the bare expectation value $\langle\Psi_n|\hat{H}|\Psi_n\rangle$. In step 4, we compute the energy expectation value $E(\theta)$ using the analytical equation derived in reference 15.[15] In step 5, we compute a second energy expectation value $E(\theta + d\theta)$ where $d\theta$ is determined by some predefined optimization scheme. Unless otherwise stated, we will use the simultaneous perturbation stochastic approximation (SPSA).[43] In step 6, we compute $g = \alpha[E(\theta + d\theta) - E(\theta)]$ where α is the predefined learning rate. It is common practice to have an α change during the optimization. Unless otherwise stated, at a given iteration k, we set

$$\alpha = a\frac{(k+1)^\gamma}{(A+k+1)^\beta} \tag{13}$$

with $a = 0.0625$ (Ha^{1-}), $\gamma = 0.101$, $\beta = 0.201$, and $A = 10$. These values are selected because they tend to provide the fastest optimization without reducing the accuracy of the final energies. In step 7, we check whether the energy has converged by comparing g to a predefined tolerance ϵ. In practice, ϵ is often chosen after optimization has been run for a specified number of iterations in order to get a sense of the variance in the data. If the energy has converged, then the algorithm is terminated and $E(\theta)$ is returned. If the energy has not converged, then we return to step 4 with an updated set of parameters.

3. RESULTS AND DISCUSSION

We demonstrate an algorithm for the water molecule. Herein, we consider a 1s orbital for each hydrogen atom and 1s, 2s, and 2p orbitals for the oxygen atom. These orbitals are described by using the minimal STO-3G basis set provided in Psi4. We then performed classical HF calculations to obtain the HF orbitals. We obtain the Hamiltonian coefficients h_{pq}^1, h_{pq}^{2D}, and h_{pqrs}^{2F}, describing the HF orbital interactions, by calculating the Hamiltonian integrals using OpenFermion with the Psi4 plugin.[44,45] The water molecule and its orbital energy levels are depicted in Figure 1. The geometry of the water molecule is set such that the oxygen is at the origin and the hydrogen atoms

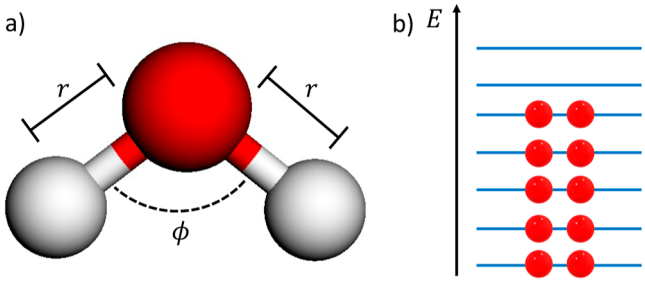

Figure 1. Water molecule specifications. (a) Geometry of the water molecule. The geometry is characterized by the distance r between the hydrogen atoms and the oxygen atom and the angle ϕ between the hydrogen atoms. Throughout, we set $\phi = 104.5°$, which is the known optimal angle for water. The equilibrium distance is $r = 0.9584$ Å; however, r is varied below. (b) Orbital occupation. The red balls represent electrons and the blue lines represent energy levels in the HF basis. We consider all 14 orbitals of the water molecule and the orbitals are filled with 10 electrons.

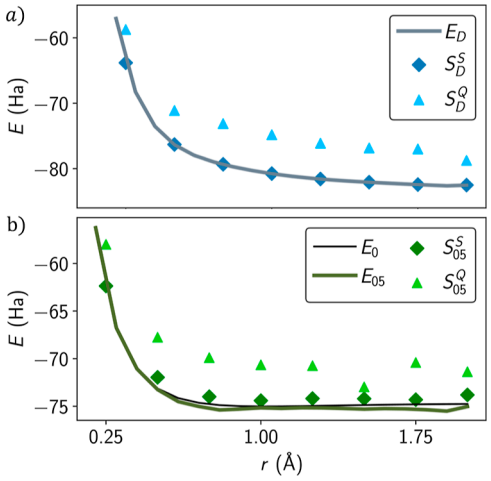

Figure 2. Energy expectation value using the single-parameter ansatz. (a) Data for $\hat{H}_D = \hat{H}_1 + \hat{H}_{2D}$. The solid gray curve E_D is the ground-state energy of $\hat{H}_D$ found using direct diagonalization, the blue diamonds S_D^S are obtained from a noise-free simulation of our method, and the light-blue triangles S_D^Q are obtained from QC runs. (b) Data for the FCI Hamiltonian except that Pauli terms with weight less than 0.05 Ha are cut. The solid black curve E_0 is the exact ground-state energy of the FCI Hamiltonian, the solid green curve E_{05} is from direct diagonalization of the Hamiltonian cut at 0.05 Ha, the green diamonds S_{05}^S are obtained from a noise-free simulation of our method, and the light-green triangles S_{05}^Q are obtained from QC runs. Note that E_D is unbounded but E_0 is bounded. The bounding can be seen more clearly in Figure 8.

https://doi.org/10.1021/acsomega.4c01642
ACS Omega 2024, 9, 21353−21364

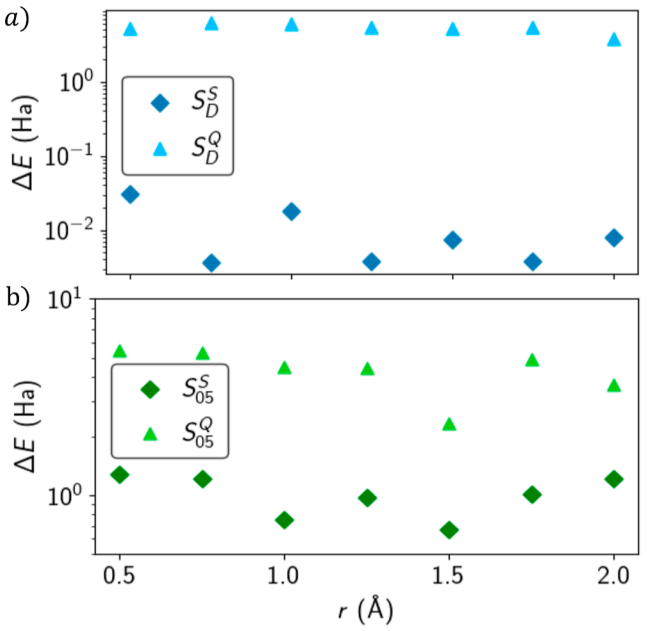

Figure 3. Difference in the energy expectation value between the energy from direct diagonalization and from the single-parameter ansatz. (a) Data for $\hat{H}_D = \hat{H}_1 + \hat{H}_{2D}$. The energies are compared to E_D from Figure 2a. The blue diamonds S_D^S are obtained from a noise-free simulation of our method and the light-blue triangles S_D^Q are obtained from QC runs. (b) Data for the FCI Hamiltonian except that Pauli terms with weight less than 0.05 Ha are cut. The energies are compared to E_{05} Figure 2b. The green diamonds S_{05}^S are obtained from a noise-free simulation of our method, and the light-green triangles S_{05}^Q are obtained from QC runs. The energy differences in both plots are plotted on a log scale.

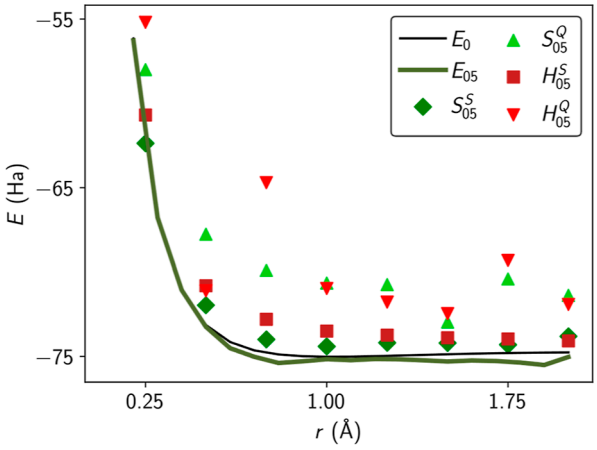

Figure 4. Energy expectation value for the Hamiltonian cut at 0.05 Ha. The solid black curve E_0 is the ground-state energy for the FCI Hamiltonian calculated using direct diagonalization. The green diamonds S_{05}^S are from a noise-free simulation of the single-parameter ansatz. The light-green triangles S_{05}^Q are from QC runs of the single-parameter ansatz. The red squares H_{05}^S are from a noise-free simulation of the HE ansatz. The light-red inverted triangles H_{05}^Q are from QC runs of the HE ansatz.

are at $x_1 = \pm\, r \sin\phi/2$, $y_1 = -r\cos\phi/2$, and $z_1 = 0$. Each hydrogen atom contributes 1 electron. The oxygen atom contributes 8 electrons. In total, there are 14 orbitals and 10 electrons. We use the JW transformation to decompose the Hamiltonian as a sum of Pauli terms. We use the construction in

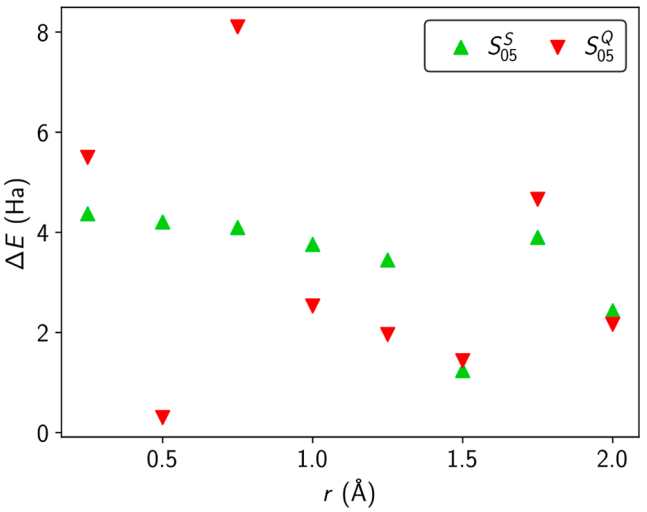

Figure 5. Difference in the energy expectation value between the simulated data and the data obtained from the quantum computer. The light-green triangles S_{05}^Q show the difference between QC runs of the single-parameter ansatz and noise-free simulations of the single-parameter ansatz. The light-red inverted triangles H_{05}^Q show the difference between QC runs of the HE ansatz and noise-free simulations of the HE ansatz.

reference 15[15] to transform the Thouless operator into a quantum circuit. These transformations map the 14 orbitals onto 14 qubits. The electron number is fixed by the initial state, and the ansatz does not change the particle number.

3.1. Using a Single Variational Parameter. Let us define the single-parameter ansatz

$$\hat{D}(\theta) = \exp(-\theta \hat{H}_{2D}) \tag{14}$$

This single-parameter ansatz can be thought of as a modification to the Gutzwiller ansatz, which is known to capture the lowest-order effects of the electron−electron interactions. In Figure 2, we plot the energy expectation value results from CVQE using the single-parameter ansatz for the water molecule, and in Figure 3, we plot the difference between the energy results and the energy from direct diagonalization. The optimization parameter θ is scanned from $\theta_i = -2$ Ha^{1-} to $\theta_f = 2$ Ha^{1-} with a step size of $d\theta = 0.1$ Ha^{1-}. The E_D data in Figure 2a shows the ground-state energy of $\hat{H}_D = \hat{H}_1 + \hat{H}_{2D}$ calculated using direct diagonalization. The data S_D^S represent a noise-free simulation of the CVQE procedure for $\hat{H}_D$. For S_D^S, the minimum value of θ is found to be $\theta^* = 0.2$ Ha^{1-} for all values of r. The energies in S_D^S have errors of less than 0.03 Ha. The high accuracy of the single-parameter ansatz, in this case, is expected because the two-body interactions that are included in $\hat{H}_D$ are completely captured by $\hat{H}_{2D}$. Thus, we expect the two-body interactions to alter the ground state according to an operator of the form (14) when there are no off-diagonal interactions.

The curve E_0 in Figure 2b shows the ground-state energy for the FCI Hamiltonian found by direct diagonalization. The remainder of the data in Figure 2b corresponds to the Hamiltonian cut such that Pauli terms with weights less than 0.05 Ha are not included. See Appendix A for an explanation of the cut. The data S_{05}^S show the results from running a noise-free simulation for cut at 0.05 Ha. For S_{05}^S, the minimum values of θ are found to be in the range 0 Ha^{1-} < θ^* < 1 Ha^{1-}. The energies in S_{05}^S have errors near 1 Ha.

https://doi.org/10.1021/acsomega.4c01642
ACS Omega 2024, 9, 21353−21364

Table 2. Number of Circuit Executions for the Simulations. From Left to Right, the Columns Represent the Distance r between the Oxygen and Hydrogen Atoms, the Number of Shots, the Number of Pauli Terms in the Hamiltonian, the Number of Iterations Required to Converge VQE, the Total Number of Circuit Executions for VQE, and the Total Number of Circuit Executions for CVQE

r (Å)	shots	Pauli terms	iterations	N_{VQE}	N_{CVQE}
0.25	1024	134	300	8.2×10^7	1.4×10^5
0.50	1024	150	152	4.7×10^7	1.5×10^5
0.75	1024	154	289	9.1×10^7	1.6×10^5
1.00	1024	162	278	9.2×10^7	1.7×10^5
1.25	1024	162	278	9.2×10^7	1.7×10^5
1.50	1024	166	289	9.8×10^7	1.7×10^5
1.75	1024	170	246	8.6×10^7	1.7×10^5
2.00	1024	170	253	8.8×10^7	1.7×10^5

Table 3. Number of Circuit Executions for the QC Data. From Left to Right, the Columns Represent the Distance r between the Oxygen and Hydrogen Atoms, the Number of Shots, the Number of Pauli Terms in the Hamiltonian, the Number of Iterations Required to Converge QC Runs of VQE, the Total Number of Circuit Executions Used during the QC Runs of VQE, and the Total Number of Circuit Executions Used for QC Runs of CVQE

r (Å)	shots	Pauli terms	iterations	N_{VQE}	N_{CVQE}
0.25	1024	134	189	5.2×10^7	1.4×10^5
0.50	1024	150	205	6.3×10^7	1.5×10^5
0.75	1024	154	122	3.8×10^7	1.6×10^5
1.00	1024	162	71	2.4×10^7	1.7×10^5
1.25	102f4	162	80	2.7×10^7	1.7×10^5
1.50	1024	166	68	2.3×10^7	1.7×10^5
1.75	1024	170	54	1.9×10^7	1.7×10^5
2.00	1024	170	69	2.4×10^7	1.7×10^5

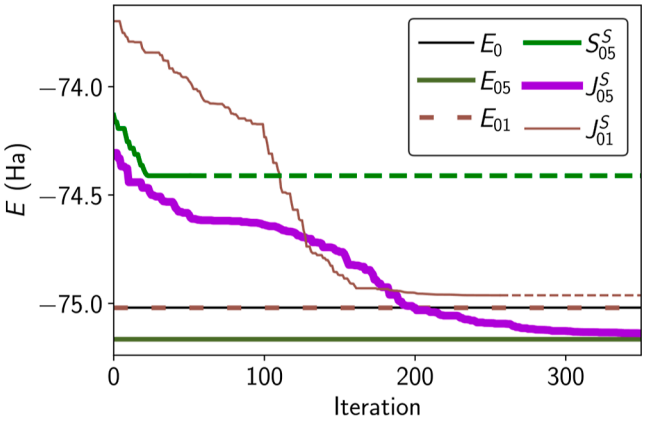

Figure 6. Energy as a function of the optimization iterations of various noise-free simulations. The thin black line E_0 is the FCI ground-state energy. The dark-green line E_{05} is the ground-state energy for the Hamiltonian cut at 0.05 Ha, found using direct diagonalization. The green curve S^S_{05} is data from the single-parameter ansatz with the Hamiltonian cut at 0.05 Ha. The thick purple curve J^S_{05} is the Jastrow ansatz with the Hamiltonian cut at 0.05 Ha. The thin brown line J^S_{01} is the Jastrow ansatz with the Hamiltonian cut at 0.01 Ha. The dashed brown line E_{01} is the ground-state energy for the Hamiltonian cut at 0.01 Ha, found using direct diagonalization. Other dashed lines indicate extrapolations of data that has converged.

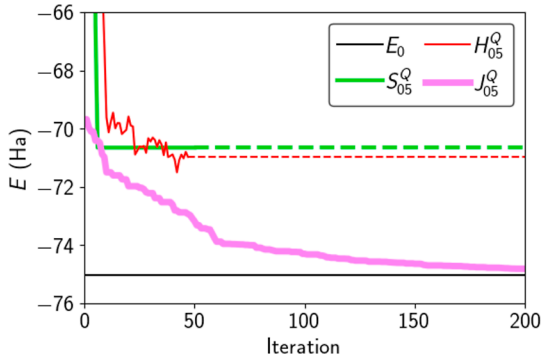

Figure 7. Energy as a function of the optimization iterations of various QC runs with a Hamiltonian cut at 0.05 Ha. The black line E_0 is the ground-state energy for the FCI Hamiltonian calculated using direct diagonalization. The light-green curve S^Q_{05} is the single-parameter ansatz. The thin light-red curve H^Q_{05} is the HE ansatz. The thick pink curve J^Q_{05} is the Jastrow ansatz. Dashed lines indicate extrapolations of data that has converged.

Thus, we find that when there are no off-diagonal many-body terms, the single-parameter ansatz is very accurate. However, when $\hat{H}_{2F}$ is included, there is error. This is due to the ground state living outside of the manifold that the single-parameter ansatz can access.

In Figure 2, S^Q_D and S^Q_{05} represent QC data. For S^Q_D, the minimum value of θ is found to be $\theta^* = -0.05$ Ha^{1-} for all values of r. For S^Q_{05}, the minimum values of θ are found to be in the range -1 Ha$^{1-} < \theta^* < 0$ Ha^{1-}. The difference in the optimal values of θ between the quantum data and the simulated data suggests that the parameter adjusts for the errors due to QC noise. Indeed, the errors are much less than expected given the reported gate errors on the device which are between 0.5 and 2% per CNOT gate. In the next section, we will compare the quantum errors in CVQE to those found in VQE to get a better understanding of how the QC noise accumulates with gate number.

3.2. Comparison to the HE Ansatz. We compare the results obtained from CVQE to those obtained from VQE. It is not trivial to use the Jastrow ansatz with VQE; therefore, we use

https://doi.org/10.1021/acsomega.4c01642
ACS Omega 2024, 9, 21353−21364

Table 4. Specifications of IBMQ Hanoi Based on the Date the Data Was Taken

physical qubit	q_{25}	q_{22}	q_{19}	q_{16}	q_{14}	q_{13}	q_{12}	q_{10}	q_7	q_4	q_1	q_2	q_3	q_5
frequency (GHz)	4.81	4.92	5.0	4.88	5.05	4.96	4.72	4.82	4.92	5.07	5.16	5.26	5.1	5.21
T1 (μs)	233.5	194.7	161.0	193.9	160.6	277.9	266.0	211.1	218.2	153.3	106.6	155.9	117.0	144.9
T2 (μs)	99.9	85.3	236.5	191.1	25.0	322.7	198.6	234.6	239.8	20.7	102.5	183.6	32.1	187.2
readout error (%)	1.11	3.04	0.64	1.01	0.93	5.67	1.75	2.42	1.21	1.01	1.14	1.72	1.66	0.67
$\sqrt{X}$ error (%)	0.017	0.019	0.014	0.031	0.021	0.019	0.021	0.022	0.012	0.026	0.031	0.053	0.122	0.019
$CX_{q0,qi}$ error		0.811												
$CX_{q1,qi}$ error	0.811		0.815											
$CX_{q2,qi}$ error		0.815		0.669										
$CX_{q3,qi}$ error			0.669		2.358									
$CX_{q4,qi}$ error				2.358		0.563								
$CX_{q5,qi}$ error					0.563		0.491							
$CX_{q6,qi}$ error						0.491		0.794						
$CX_{q7,qi}$ error							0.794		0.565					
$CX_{q8,qi}$ error								0.565		1.085				
$CX_{q9,qi}$ error									1.085		0.562			
$CX_{q10,qi}$ error										0.562		0.571		
$CX_{q11,qi}$ error											0.571		1.878	
$CX_{q12,qi}$ error												1.878		1.131
$CX_{q13,qi}$ error													1.131	

the HE ansatz. Each HE ansatz layer is built from a layer of CNOT gates connecting every neighboring qubit (on the hardware level) and a layer of R^Y gates (single qubit rotations around the y-axis of the Bloch sphere) acting on every qubit. There is a variation of the parameter for each R^Y gate. We use SPSA as our optimizer for VQE. We start the optimization using random angles, which tends to improve the final energies, see Appendix C. We find that for more than 2 layers of the HE ansatz, the energy expectation value does not converge within 300 iterations. Therefore, we restricted the algorithm to 2 layers.

Figure 4 shows a comparison of the energy expectation values obtained from a 2-layer HE ansatz using VQE and the single-parameter ansatz using CVQE. Figure 5 shows the differences in energy between the data obtained from the simulations and the quantum computer. The data S^S_{05} and H^S_{05} represent results from the noise-free simulation for the single-parameter ansatz and the HE ansatz, respectively. We find that the single-parameter ansatz provides an energy closer to the true ground-state energy than the HE ansatz. This is remarkable as the 2-layer HE ansatz has 28 variational parameters. The accuracy of the single-parameter ansatz demonstrates the advantage of using a physically motivated ansatz.

The S^Q_{05} and H^Q_{05} in Figures 4 and 5 represent QC data for the single-parameter ansatz and the HE ansatz, respectively. The energy differences from the QC data for the single-parameter ansatz and the HE ansatz are comparable. This is remarkable as the 2-layer HE ansatz has only 26 CNOT gates, while our construction of the Thouless operator contains 364 CNOT gates. Furthermore, the CNOT error for the IBM quantum computers we used ranges between about 0.5 and 2%. With 364 CNOT gates each applying 0.5% error, we would not expect any useable results. The relatively high fidelity of our approach can be explained by the postprocessing in CVQE. Because CVQE adjusts the probability distribution after the quantum measurements are taken, some of the QC noise is effectively removed during the classical optimization step. This could be a major advantage for CVQE.

Another advantage of the CVQE algorithm is the low number of required circuit executions. In Table 2, we show the total number of circuit executions used during the simulations of both CVQE and VQE. The number of executions required for VQE is $N_{\mathrm{VQE}} = 2 \times \text{shots} \times \text{Pauli terms} \times \text{iterations}$. For CVQE, the iterations are performed classically; thus, the number of circuit executions is only $N_{\mathrm{CVQE}} = \text{shots} \times \text{Pauli terms}$. The factor of 2 in N_{VQE} comes from the fact that we calculate two energy expectation values per iteration using SPSA. From the table, we see a 2-order-of-magnitude decrease in N_{CVQE} as compared to N_{VQE}.

Table 3 shows the number of circuit executions used during the QC execution of both VQE and CVQE. The difference in the number of circuit executions is less pronounced in the QC data. The QC noise makes it impossible to resolve fine-tuned optimization, and thus, the number of iterations until convergence is fewer.

3.3. Free Variational Parameters. We consider the full Jastrow operator (6) and allow each of the $N_\theta = (Q+1) \times Q/2 = 105$ (one for each unique operator in eq 6) variational parameters to vary independently. The full Jastrow ansatz does not introduce additional complexities for the quantum computer, and in fact, the same measurement results are used for the full Jastrow ansatz as were used for the single-parameter ansatz. In Figure 6, we show the energy during the optimization procedure for a noise-free simulation of CVQE. See Appendix B for a description of the optimization procedure. The data J^S_{05} show runs of the Jastrow ansatz with independent variational parameters. We find that there is a substantial improvement over the single-parameter ansatz. The difference between E_{05} and the final value of J^S_{05} is less than 0.017 Ha. This error is less than the error due to cutting the low-weight Pauli terms in the Hamiltonian. Therefore, we ran the algorithm again, including Pauli terms with weights greater than 0.01 Ha. The difference between E_0 and the final value of J^S_{01} is less than 0.05 Ha.

In Figure 7, we show the energy during the optimization procedure using the QC results. The data J^Q_{05} represent data using the Jastrow ansatz. We find that the full Jastrow ansatz outperforms both the single-parameter ansatz and the 2-layer HE ansatz by approximately an order of magnitude. The difference between E_{05} and the final value of J^Q_{05} is less than 0.14 Ha. Furthermore, the energy obtained from QC runs of the full Jastrow ansatz is closer to its noise-free simulation than is that of

https://doi.org/10.1021/acsomega.4c01642
ACS Omega 2024, 9, 21353−21364

Table 5. Specifications of IBMQ Mumbai Based on the Date the Data Was Taken

physical qubits	q_1	q_4	q_7	q_{10}	q_{12}	q_{15}	q_{18}	q_{21}	q_{23}	q_{24}	q_{25}	q_{22}	q_{19}	q_{20}
frequency (GHz)	4.93	5.02	4.89	4.96	4.74	4.85	4.78	4.93	4.88	4.67	4.76	4.91	4.82	5.04
T1 (μs)	183.7	104.0	128.2	114.3	182.3	184.5	136.4	76.6	74.8	152.3	217.5	50.8	148.3	143.1
T2 (μs)	89.7	36.7	89.2	262.9	190.9	187.8	149.9	98.4	22.1	65.5	64.9	65.1	246.5	131.0
readout error (%)	1.25	1.75	1.67	1.52	3.06	1.79	6.23	3.09	8.26	3.91	1.71	1.11	1.76	1.43
$\sqrt{X}$ error (%)	0.016	0.027	0.022	0.02	0.015	0.018	0.021	0.028	0.056	0.036	0.02	0.023	0.021	0.018
$CX_{q0,qi}$ error		0.846												
$CX_{q1,qi}$ error	0.846		1.327											
$CX_{q2,qi}$ error		1.327		0.757										
$CX_{q3,qi}$ error			0.757		0.536									
$CX_{q4,qi}$ error				0.536		0.839								
$CX_{q5,qi}$ error					0.839		0.751							
$CX_{q6,qi}$ error						0.751		0.657						
$CX_{q7,qi}$ error							0.657		1.248					
$CX_{q8,qi}$ error								1.248		2.067				
$CX_{q9,qi}$ error									2.067		0.562			
$CX_{q10,qi}$ error										0.562		0.616		
$CX_{q11,qi}$ error											0.616		0.681	
$CX_{q12,qi}$ error												0.681		0.542
$CX_{q13,qi}$ error													0.542	

Table 6. Specifications of IBMQ Guadalupe Based on the Date the Data Was Taken

physical qubit	q_{15}	q_{10}	q_7	q_4	q_1	q_2	q_3	q_5	q_8	q_9	q_{11}	q_{14}	q_{13}	q_{12}
frequency (GHz)	5.13	5.43	5.2	5.35	5.16	5.31	5.47	5.3	5.17	5.25	5.39	5.2	5.04	5.26
T1 (μs)	88.4	77.9	127.1	35.8	98.2	49.9	109.9	139.3	134.3	100.3	75.2	69.8	154.3	86.5
T2 (μs)	115.9	124.0	138.7	63.8	136.6	76.1	152.4	109.8	145.6	74.2	81.5	104.7	105.9	145.7
readout error (%)	1.62	3.4	1.8	2.42	1.42	1.79	1.51	1.47	2.07	2.18	2.36	1.95	1.02	1.59
$\sqrt{X}$ error (%)	0.022	0.02	0.019	0.294	0.033	0.036	0.025	0.032	0.022	0.031	0.089	0.026	0.021	0.02
$CX_{q0,qi}$ error														0.61
$C_{Xq1,qi}$ error			0.557											1.424
$CX_{q2,qi}$ error		0.557		6.328										
$CX_{q3,qi}$ error			6.328		1.759									
$CX_{q4,qi}$ error				1.759		0.962								
$CX_{q5,qi}$ error					0.962		1.261							
$CX_{q6,qi}$ error						1.261		1.116						
$CX_{q7,qi}$ error							1.116		0.571					
$CX_{q8,qi}$ error								0.571		0.789	0.92			
$CX_{q9,qi}$ error									0.789					
$CX_{q10,qi}$ error									0.92			1.229		
$CX_{q11,qi}$ error											1.229		0.954	
$CX_{q12,qi}$ error												0.954		0.57
$CX_{q13,qi}$ error	0.61	1.424											0.57	

the single-parameter ansatz. This is expected as increasing the number of free variational parameters increases the ability of the classical optimization procedure to mitigate QC errors.

4. CONCLUSIONS

We have demonstrated that CVQE, using the Jastrow ansatz, is an effective algorithm for studying the water molecule. As we have not tailored our algorithm based on any of the symmetry properties of the water molecule, we expect our method to be effective for molecules in general.

Furthermore, we have demonstrated that CVQE has a number of advantages over VQE. For one, CVQE requires orders of magnitude fewer QC executions. This is especially important for molecular Hamiltonians, which can contain thousands of Pauli terms, even for small molecules. Second, we find that the postprocessing in CVQE provides robustness to quantum hardware errors. This allows the quantum part of the algorithm to contain many more gates than are otherwise possible.

The results of this work demonstrate that CVQE is particularly suited for near-term QC studies of molecules, where the QC noise is high and resources are limited. As quantum hardware continues to improve, studying larger molecules will become practical.

APPENDIX A

Cutting Pauli Terms

The Hamiltonian cut in the main text is made to reduce the number of Pauli terms in order to improve the run time of the optimization. As we are limited to two-body interactions, the number of Pauli terms does not grow exponentially but it can still be a bottleneck for large systems. For the water molecule, we have nearly 3000 Pauli terms in $\hat{H}_{2F}$. Cutting the terms that have weights less than 0.05 Ha reduces the number of terms to around

https://doi.org/10.1021/acsomega.4c01642
ACS Omega 2024, 9, 21353−21364

Table 7. Specifications of IBMQ Kolkata Based on the Date the Data Was Taken

physical qubit	q_{22}	q_{25}	q_{24}	q_{23}	q_{21}	q_{18}	q_{15}	q_{12}	q_{13}	q_{14}	q_{11}	q_{8}	q_{5}	q_{3}
frequency (GHz)	5.12	4.92	5.0	5.14	5.27	5.09	5.03	4.96	5.02	5.12	4.88	4.96	5.1	4.87
T1 (μs)	136.8	191.7	76.1	159.4	83.4	137.3	82.2	195.5	171.4	170.4	15.4	144.3	95.3	104.6
T2 (μs)	38.8	168.1	32.0	163.9	94.6	87.9	157.4	90.3	224.2	132.2	18.4	133.8	40.4	57.6
readout error (%)	1.44	0.84	0.72	0.69	0.63	0.78	0.96	1.12	0.94	0.66	4.68	1.44	2.41	3.71
$\sqrt{X}$ error (%)	0.028	0.017	0.056	0.018	0.021	0.015	0.026	0.049	0.027	0.019	0.153	0.013	0.017	0.146
$CX_{q0,qi}$ error		0.517												
$CX_{q1,qi}$ error	0.517		100											
$CX_{q2,qi}$ error		100		0.548										
$CX_{q3,qi}$ error			0.548		0.5									
$CX_{q4,qi}$ error				0.5		0.663								
$CX_{q5,qi}$ error					0.663		1.174							
$CX_{q6,qi}$ error						1.174		0.588						
$CX_{q7,qi}$ error							0.588		0.697					
$CX_{q8,qi}$ error								0.697		0.565				
$CX_{q9,qi}$ error									0.565		4.883			
$CX_{q10,qi}$ error										4.883		1.979		
$CX_{q11,qi}$ error											1.979		0.603	
$CX_{q12,qi}$ error												0.603		2.064
$CX_{q13,qi}$ error													2.064	

Table 8. Specifications of IBMQ Washington Based on the Date the Data Was Taken

physical qubit	q_{43}	q_{34}	q_{24}	q_{25}	q_{26}	q_{27}	q_{28}	q_{29}	q_{30}	q_{31}	q_{32}	q_{36}	q_{51}	q_{50}
frequency (GHz)	5.03	4.94	4.77	4.87	5.0	5.08	5.2	4.99	5.08	5.13	5.2	5.1	5.21	5.02
T1 (μs)	103.9	78.2	142.6	136.3	92.8	146.0	109.5	81.3	136.7	63.0	92.4	125.5	118.9	99.9
T2 (μs)	135.2	138.3	156.5	119.1	164.6	60.4	90.4	18.7	172.2	58.4	32.0	128.4	87.4	174.8
readout error (%)	2.92	2.41	4.69	0.84	0.24	5.1	0.33	0.81	0.23	0.31	0.29	0.69	0.46	5.86
$\sqrt{X}$ error (%)	0.025	0.027	0.328	0.023	0.056	0.024	0.022	0.022	0.038	0.035	0.025	0.043	0.023	0.025
$CX_{q0,qi}$ error		1.041												
$CX_{q1,qi}$ error	1.041		2.54											
$CX_{q2,qi}$ error		2.54		0.973										
$CX_{q3,qi}$ error			0.973		0.729									
$CX_{q4,qi}$ error				0.729		0.845								
$CX_{q5,qi}$ error					0.845		1.454							
$CX_{q6,qi}$ error						1.454		0.653						
$CX_{q7,qi}$ error							0.653		0.81					
$CX_{q8,qi}$ error								0.81		0.779				
$CX_{q9,qi}$ error									0.779		0.798			
$CX_{q10,qi}$ error										0.798		0.819		
$CX_{q11,qi}$ error											0.819		0.838	
$CX_{q12,qi}$ error												0.838		0.711
$CX_{q13,qi}$ error													0.711	

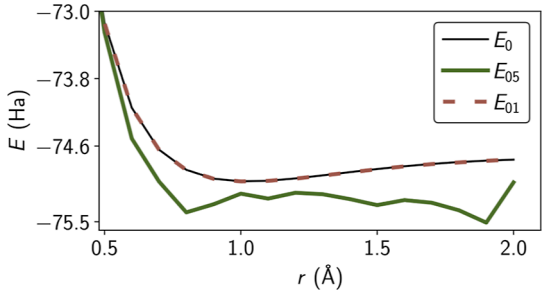

Figure 8. Ground-state energy calculated using direct diagonalization as a function of r. The thin black line E_0 is the FCI ground-state energy. The thick dark-green line E_{05} is for a cut at 0.05 Ha. The dashed brown line E_{01} is for a cut at 0.01 Ha.

300. This cut tends to cause large errors in the ground-state energy; however, these errors are much less than the errors due to the QC noise. As quantum hardware improves, we can reduce the cut value so that the QC noise is always the dominant source of error. With the absence of QC noise, as the cutoff is reduced to zero, the results will converge to the FCI results. Cutting the terms that have weight less than 0.01 Ha only reduces the number of terms to around 1500 but the ground-state energy is nearly identical to the FCI ground state. Figure 8 shows the ground-state energy calculated by diagonalizing the Hamiltonian cut at 0, 0.05, and 0.01 Ha. The error from cutting at 0.05 Ha is smaller than the error from using the single-parameter ansatz. The error from cutting at 0.01 Ha is smaller than the error from using the full Jastrow ansatz.

APPENDIX B

Optimizer

For CVQE, we modified the SPSA in the following way. In SPSA, two near but arbitrarily different parameter sets are

https://doi.org/10.1021/acsomega.4c01642
ACS Omega 2024, 9, 21353−21364

Table 9. Specifications of IBMQ Montreal Based on the Date the Data Was Taken

physical qubits	q_3	q_5	q_8	q_{11}	q_{14}	q_{13}	q_{12}	q_{15}	q_{18}	q_{21}	q_{23}	q_{24}	q_{25}	q_{26}
frequency (GHz)	5.1	5.03	4.91	5.03	4.96	4.87	4.97	5.03	4.98	5.07	4.97	5.05	4.93	5.0
T1 (μs)	75.6	131.0	112.0	105.7	97.5	99.6	58.0	111.0	80.5	101.2	144.8	109.5	95.3	92.9
T2 (μs)	65.4	98.5	142.3	51.7	97.1	68.9	66.8	130.6	27.3	49.0	38.7	64.0	77.7	165.1
readout error (%)	1.11	2.09	1.48	1.27	0.98	0.71	3.27	2.05	3.23	2.19	9.67	3.96	0.83	0.98
$\sqrt{X}$ error (%)	0.026	0.033	0.019	0.025	0.022	0.016	0.025	0.027	0.037	0.047	0.023	0.022	0.029	0.045
$CX_{q0,qi}$ error		0.915												
$CX_{q1,qi}$ error	0.915		0.651											
$CX_{q2,qi}$ error		0.651		0.74										
$CX_{q3,qi}$ error			0.74		0.559									
$CX_{q4,qi}$ error				0.559		0.735								
$CX_{q5,qi}$ error					0.735		0.7							
$CX_{q6,qi}$ error						0.7		1.204						
$CX_{q7,qi}$ error							1.204		1.186					
$CX_{q8,qi}$ error								1.186		1.327				
$CX_{q9,qi}$ error									1.327		0.791			
$CX_{q10,qi}$ error										0.791		0.947		
$CX_{q11,qi}$ error											0.947		0.871	
$CX_{q12,qi}$ error												0.871		0.692
$CX_{q13,qi}$ error													0.692	

Table 10. Specifications of IBMQ Toronto Based on the Date the Data Was Taken

physical qubits	q_6	q_7	q_4	q_1	q_2	q_3	q_5	q_8	q_{11}	q_{14}	q_{13}	q_{12}	q_{15}	q_{18}
frequency (GHz)	5.15	4.92	5.09	5.0	5.14	5.21	5.17	5.03	5.12	5.02	5.13	4.93	5.09	5.06
T1 (μs)	82.7	138.8	117.4	125.8	94.1	112.2	119.6	117.0	127.7	125.5	111.1	98.6	102.3	94.0
T2 (μs)	56.8	196.1	124.9	126.8	117.4	153.9	184.7	133.7	207.7	233.8	137.5	143.4	60.5	116.3
readout error (%)	8.61	3.59	4.58	3.76	0.98	1.26	1.18	1.48	1.16	1.34	21.06	7.93	27.45	1.57
$\sqrt{X}$ error (%)	0.032	0.017	0.018	0.035	0.028	0.05	0.032	0.026	0.025	0.02	0.028	0.252	0.112	0.146
$CX_{q0,qi}$ error		0.629												
$CX_{q1,qi}$ error	0.629		0.875											
$CX_{q2,qi}$ error		0.875		0.727										
$CX_{q3,qi}$ error			0.727		1.265									
$CX_{q4,qi}$ error				1.265		0.779								
$CX_{q5,qi}$ error					0.779		0.917							
$CX_{q6,qi}$ error						0.917		0.776						
$CX_{q7,qi}$ error							0.776		0.571					
$CX_{q8,qi}$ error								0.571		0.908				
$CX_{q9,qi}$ error									0.908		0.904			
$CX_{q10,qi}$ error										0.904		3.307		
$CX_{q11,qi}$ error											3.307		2.016	
$CX_{q12,qi}$ error												2.016		1.886
$CX_{q13,qi}$ error													1.886	

chosen. The parameters are then adjusted proportional to the energy difference from the two parameter sets. We find that simply choosing the better parameter set as the updated set shows better convergence. In this way, energy never increases. We initialize the optimization using random angles.

APPENDIX C

Initialization of VQE Angles

In the main text, we use randomly initialized angles for the HE ansatz. This was chosen because random angles tend to produce better final energies than initializing to the HF state. Figure 9 shows the optimized energies using both random initial angles and angles initialized to the HF state. We see that the randomly initialized angles perform better.

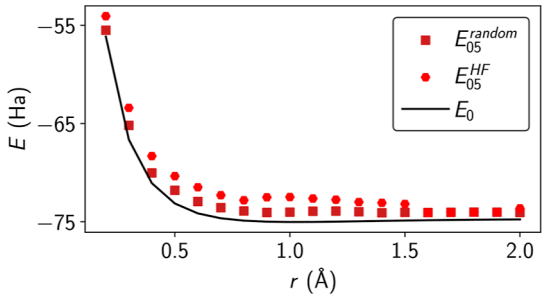

Figure 9. Ground-state energy calculated using the VQE with the HE ansatz as a function of r. The thin black line E_0 is the FCI ground-state energy. The dark-red squares E_{05}^{random} are for a cut at 0.05 Ha using random initialized angles for the HE ansatz. The light-red hexagons E_{05}^{HF} are for a cut at 0.05 Ha using angles initialized to the HF state.

https://doi.org/10.1021/acsomega.4c01642
ACS Omega 2024, 9, 21353−21364

APPENDIX D

Hamiltonian Hierarchies

In the main text, we claim that the $\sum_{pq}|h^{1}_{pq}| > \sum_{pq}|h^{2D}_{pq}| > \sum_{pqrs} h^{2F}_{pqrs}$. In Figure 10, we plot each of these terms. We see that the inequalities do indeed hold over the range of r values used in the main text.

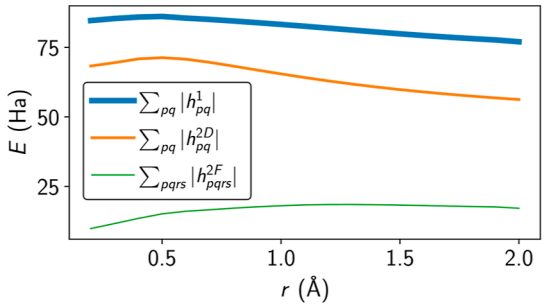

Figure 10. Strength of each Hamiltonian as a function of r. The thick blue line is for $\hat{H}_1$, the orange line is for $\hat{H}_{2D}$, and the thin green line is for $\hat{H}_{2F}$.

APPENDIX E

Single-Parameter Scans

In Figure 11, we show plots of the energy as a function of the parameter in the single-parameter ansatz. Often, there is a large

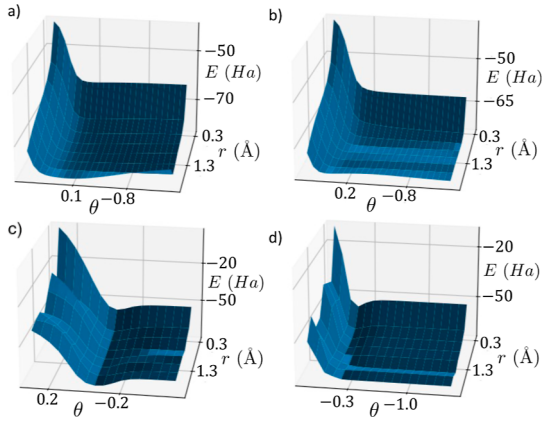

Figure 11. Scans of energy as a function of the parameter in the single-parameter ansatz at different values of r. (a) Simulations for the $\hat{H}_D$ Hamiltonian. (b) Simulations for the Hamiltonian cut at 0.05 Ha. (c) Quantum data for the $\hat{H}_D$ Hamiltonian. (d) Quantum data for the Hamiltonian cut at 0.05 Ha.

range in the parameter values where the energy is relatively flat. The fact that the reported optimal value for the $\hat{H}_D$ scans is the same for all r is likely due to the discretization of θ. With a smaller step size, we expect the optimal value to vary slightly.

APPENDIX F

Bare Thouless Energies

In Figure 12, we plot the energies obtained from the QC runs including the unoptimized energies calculated by applying the Thouless operator and taking the energy expectation value of the resulting quantum state. We see that the single-parameter ansatz

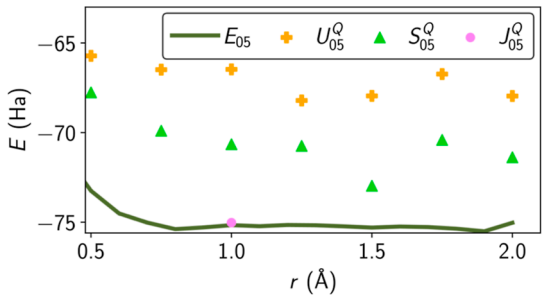

Figure 12. Energy expectation values from the QC including unoptimized data. The solid green curve E_{05} is from direct diagonalization of the Hamiltonian cut at 0.05 Ha; the orange plus signs are obtained from QC runs without applying any postprocessing optimization; the light-green triangles $S_{05}{}^{Q}$ are obtained using the single-parameter ansatz; the pink circle is obtained from the full Jastrow ansatz. We ran the full Jastrow ansatz for only a single r value as the calculations take weeks to complete.

shows significant improvement over the unoptimized data. Furthermore, the full Jastrow ansatz applied an order of magnitude's improvement over the unoptimized data.

APPENDIX G

Device Specifications

We chose the backend with the shortest queue for each job. Because CVQE requires only a single QC run, we were able to collect all of the data for CVQE in a single job, which was run on IBM Hanoi. This data was used in both the single-parameter ansatz and the full Jastrow ansatz for all values of r.

For VQE, each optimization step requires a new QC run. Thus, we ran each value of r as a separate job. The data for r = 0.25, r = 1.0, and r = 1.5 was obtained from IBM Montreal. The data for r = 0.5 was obtained from IBM Mumbai. The data for r = 0.75 was obtained from IBM Guadalupe. The data for r = 1.25 was taken from IBM Kolkata. The data for r = 1.75 was obtained from IBM Toronto. The data for r = 2.0 was taken from IBM Washington.

In (Tables 4−10), the physical qubits refer to the actual qubits on the chip and they are presented in the order in which the orbitals are mapped. When transpiling the circuits to the quantum chip, the qubit indices are mapped using the built-in Qiskit transpiler. The $CX_{q_i q_j}$ gates represent controlled NOT gates controlled by logical qubit q_i and targeting logical qubit q_j.

AUTHOR INFORMATION

Corresponding Author

John P. T. Stenger − *U.S. Naval Research Laboratory, Washington, District of Columbia 20375, United States;* orcid.org/0000-0003-2184-2883; Email: john.stenger@nrl.navy.mil

Authors

C. Stephen Hellberg − *U.S. Naval Research Laboratory, Washington, District of Columbia 20375, United States;* orcid.org/0000-0002-3550-9750

Daniel Gunlycke − *U.S. Naval Research Laboratory, Washington, District of Columbia 20375, United States*

Complete contact information is available at: https://pubs.acs.org/10.1021/acsomega.4c01642

https://doi.org/10.1021/acsomega.4c01642
ACS Omega 2024, 9, 21353−21364

Notes

The authors declare no competing financial interest.

■ ACKNOWLEDGMENTS

This work has been supported by the Office of Naval Research (ONR) through the U.S. Naval Research Laboratory (NRL). We acknowledge QC resources from IBM through a collaboration with the Air Force Research Laboratory (AFRL).

■ REFERENCES

(1) Benioff, P. The computer as a physical system: A microscopic quantum mechanical Hamiltonian model of computers as represented by Turing machines. *J. Stat. Phys.* **1980**, *22* (5), 563−591.
(2) Feynman, R. P. Simulating physics with computers. *Int. J. Theor. Phys.* **1982**, *21* (6−7), 467−488.
(3) Peruzzo, A.; McClean, J. R.; Shadbolt, P.; Yung, M. H. H.; Zhou, X. Q. Q.; Love, P. J.; Aspuru-Guzik, A.; O'Brien, J. L. A variational eigenvalue solver on a photonic quantum processor. *Nat. Commun.* **2014**, *5*, 4213.
(4) McClean, J. R.; Romero, J.; Babbush, R.; Aspuru-Guzik, A. The theory of variational hybrid quantum-classical algorithms. *New J. Phys.* **2016**, *18* (2), 023023.
(5) O'Malley, P. J. J.; Babbush, R.; Kivlichan, I. D.; Romero, J.; McClean, J. R.; Barends, R.; Kelly, J.; Roushan, P.; Tranter, A.; Ding, N.; et al. Scalable Quantum Simulation of Molecular Energies. *Phys. Rev. X* **2016**, *6*, 031007.
(6) Kandala, A.; Mezzacapo, A.; Temme, K.; Takita, M.; Brink, M.; Chow, J. M.; Gambetta, J. M. Hardware-efficient variational quantum eigensolver for small molecules and quantum magnets. *Nature* **2017**, *549* (7671), 242−246.
(7) Wang, D.; Higgott, O.; Brierley, S. Accelerated Variational Quantum Eigensolver. *Phys. Rev. Lett.* **2019**, *122* (14), 140504.
(8) Arute, F.; Arya, K.; Babbush, R.; Bacon, D.; Bardin, J. C.; Barends, R.; Boixo, S.; Broughton, M.; Buckley, B. B.; Buell, D. A.; et al. Hartree-Fock on a superconducting qubit quantum computer. *Science* **2020**, *369* (6507), 1084−1089.
(9) Gonthier, J. F.; Radin, M. D.; Buda, C.; Doskocil, E. J.; Abuan, C. M.; Romero, J. Measurements as a roadblock to near-term practical quantum advantage in chemistry: Resource analysis. *Phys. Rev. Res.* **2022**, *4*, 033154.
(10) McArdle, S.; Endo, S.; Aspuru-Guzik, A.; Benjamin, S. C.; Yuan, X. Quantum computational chemistry. *Rev. Mod. Phys.* **2020**, *92* (1), 015003.
(11) Cerezo, M.; Arrasmith, A.; Babbush, R.; Benjamin, S. C.; Endo, S.; Fujii, K.; McClean, J. R.; Mitarai, K.; Yuan, X.; Cincio, L.; et al. Variational quantum algorithms. *Nat. Rev. Phys.* **2021**, *3* (9), 625−644.
(12) Head-Marsden, K.; Flick, J.; Ciccarino, C. J.; Narang, P. Quantum Information and Algorithms for Correlated Quantum Matter. *Chem. Rev.* **2021**, *121*, 3061−3120.
(13) Bian, T.; Murphy, D.; Xia, R.; Daskin, A.; Kais, S. Quantum computing methods for electronic states of the water molecule. *Mol. Phys.* **2019**, *117* (15−16), 2069−2082.
(14) Gunlycke, D.; Hellberg, C. S.; Stenger, J. P. T. Cascaded variational quantum eigensolver algorithm. *Phys. Rev. Res.* **2024**, *6*, 013238.
(15) Stenger, J. P. T.; Hellberg, C. S.; Gunlycke, D. Implementing Jastrow-Gutzwiller operators on a quantum computer using the cascaded variational quantum eigensolver algorithm. *Phys. Rev. A* **2023**, *107* (6), 062606.
(16) Jastrow, R. Many-Body Problem with Strong Forces. *Phys. Rev.* **1955**, *98* (5), 1479−1484.
(17) Gutzwiller, M. C. Effect of Correlation on the Ferromagnetism of Transition Metals. *Phys. Rev. Lett.* **1963**, *10*, 159−162.
(18) Brinkman, W. F.; Rice, T. M. Application of Gutzwiller's Variational Method to the Metal-Insulator Transition. *Phys. Rev. B* **1970**, *2*, 4302−4304.
(19) Vollhardt, D. Normal ^{3}He: an almost localized Fermi liquid. *Rev. Mod. Phys.* **1984**, *56*, 99−120.
(20) Anderson, P. W. The Resonating Valence Bond State in La2CuO4 and Superconductivity. *Science* **1987**, *235*, 1196−1198.
(21) Haldane, F. D. M. Exact Jastrow-Gutzwiller resonating-valence-bond ground state of the spin-12 antiferromagnetic Heisenberg chain with $1/r^2$ exchange. *Phys. Rev. Lett.* **1988**, *60*, 635−638.
(22) Shastry, B. S. Exact solution of an S = 1/2 Heisenberg antiferromagnetic chain with long-ranged interactions. *Phys. Rev. Lett.* **1988**, *60*, 639−642.
(23) Hellberg, C. S.; Mele, E. J. Phase diagram of the one-dimensional t-J model from variational theory. *Phys. Rev. Lett.* **1991**, *67*, 2080−2083.
(24) Hellberg, C. S.; Manousakis, E. Green's-function Monte Carlo for lattice fermions: Application to the $t - J$ model. *Phys. Rev. B* **2000**, *61*, 11787−11806.
(25) Capello, M.; Becca, F.; Fabrizio, M.; Sorella, S.; Tosatti, E. Variational Description of Mott Insulators. *Phys. Rev. Lett.* **2005**, *94* (2), 026406.
(26) Capello, M.; Becca, F.; Yunoki, S.; Sorella, S. Unconventional metal-insulator transition in two dimensions. *Phys. Rev. B* **2006**, *73* (24), 245116.
(27) Yunoki, S. Single-particle anomalous excitations of Gutzwiller-projected BCS superconductors and Bogoliubov quasiparticle characteristics. *Phys. Rev. B* **2006**, *74*, 180504.
(28) Edegger, B.; Muthukumar, V. N.; Gros, C. Gutzwiller−RVB theory of high-temperature superconductivity: Results from renormalized mean-field theory and variational Monte Carlo calculations. *Adv. Phys.* **2007**, *56* (6), 927−1033.
(29) Fabrizio, M. Gutzwiller description of non-magnetic Mott insulators: Dimer lattice model. *Phys. Rev. B* **2007**, *76*, 165110.
(30) Tahara, D.; Imada, M. Variational Monte Carlo Method Combined with Quantum-Number Projection and Multi-Variable Optimization. *J. Phys. Soc. Jpn.* **2008**, *77* (11), 114701.
(31) LeBlanc, J. P. F.; Antipov, A. E.; Becca, F.; Bulik, I. W.; Chan, G. K. L.; Chung, C. M.; Deng, Y.; Ferrero, M.; Henderson, T. M.; Jiménez-Hoyos, C. A.; et al. Solutions of the Two-Dimensional Hubbard Model: Benchmarks and Results from a Wide Range of Numerical Algorithms. *Phys. Rev. X* **2015**, *5* (4), 041041.
(32) Matsuzawa, Y.; Kurashige, Y. Jastrow-type Decomposition in Quantum Chemistry for Low-Depth Quantum Circuits. *J. Chem. Theory Comput.* **2020**, *16* (2), 944−952.
(33) Ferrari, F.; Becca, F.; Valentí, R. Charge density waves in kagome-lattice extended Hubbard models at the van Hove filling. *Phys. Rev. B* **2022**, *106* (8), L081107.
(34) Sokolov, I. O.; Dobrautz, W.; Luo, H.; Alavi, A.; Tavernelli, I. Orders of magnitude increased accuracy for quantum many-body problems on quantum computers via an exact transcorrelated method. *Phys. Rev. Res.* **2023**, *5*, 023174.
(35) Motta, M.; Sung, K. J.; Whaley, K. B.; Head-Gordon, M.; Shee, J. Bridging physical intuition and hardware efficiency for correlated electronic states: the local unitary cluster Jastrow ansatz for electronic structure. *ChemRxiv* **2023**, *14*, 11213−11227.
(36) Dobrautz, W., Sokolov, I. O., Liao, K., Ríos, P. L., Rahm, M., Alavi, A., et al. Ab Initio Transcorrelated Method enabling accurate Quantum Chemistry on near-term Quantum Hardware. **2023**, arXiv:2303.02007.
(37) Mazzola, G.; Ollitrault, P. J.; Barkoutsos, P. K.; Tavernelli, I. Nonunitary Operations for Ground-State Calculations in Near-Term Quantum Computers. *Phys. Rev. Lett.* **2019**, *123*, 130501.
(38) Murta, B.; Fernández-Rossier, J. Gutzwiller wave function on a digital quantum computer. *Phys. Rev. B* **2021**, *103*, L241113.
(39) Yao, Y.; Zhang, F.; Wang, C. Z.; Ho, K. M.; Orth, P. P. Gutzwiller hybrid quantum-classical computing approach for correlated materials. *Phys. Rev. Res.* **2021**, *3*, 013184.
(40) Seki, K.; Otsuka, Y.; Yunoki, S. Gutzwiller wave function on a quantum computer using a discrete Hubbard-Stratonovich transformation. *Phys. Rev. B* **2022**, *105* (15), 155119.
(41) Thouless, D. J. Stability conditions and nuclear rotations in the Hartree-Fock theory. *Nucl. Phys.* **1960**, *21*, 225−232.

https://doi.org/10.1021/acsomega.4c01642
ACS Omega 2024, 9, 21353−21364

(42) Somma, R.; Ortiz, G.; Gubernatis, J. E.; Knill, E.; Laflamme, R. Simulating physical phenomena by quantum networks. *Phys. Rev. A* **2002**, *65*, 042323.
(43) Spall, J. C. Multivariate stochastic approximation using a simultaneous perturbation gradient approximation. *IEEE Trans. Autom. Control* **1992**, *37* (3), 332−341.
(44) McClean, J. R.; Rubin, N. C.; Sung, K. J.; Kivlichan, I. D.; Bonet-Monroig, X.; Cao, Y.; Dai, C.; Fried, E. S.; Gidney, C.; Gimby, B.; et al. OpenFermion: the electronic structure package for quantum computers. *Quantum Sci. Technol.* **2020**, *5* (3), 034014.
(45) Smith, D. G. A.; Burns, L. A.; Sirianni, D. A.; Nascimento, D. R.; Kumar, A.; James, A. M.; Schriber, J. B.; Zhang, T.; Zhang, B.; Abbott, A. S.; et al. Psi4NumPy: An Interactive Quantum Chemistry Programming Environment for Reference Implementations and Rapid Development. *J. Chem. Theory Comput.* **2018**, *14* (7), 3504−3511.

https://doi.org/10.1021/acsomega.4c01642
ACS Omega 2024, 9, 21353−21364